Article

Multi-Objective Optimization of Kinetic Characteristics for the LBPRM-EHSPCS System

Yuhang Zhang [1], Gexin Chen [1,2,*], Guishan Yan [3], Boyuan Li [1], Jianxin Lu [1] and Wenguang Jiang [1]

1   School of Mechanical Engineering, Yanshan University, Qinhuangdao 066004, China; zhangyuhangcm@stumail.ysu.edu.cn (Y.Z.); 17692147244@163.com (B.L.); jxlu@stumail.ysu.edu.cn (J.L.); wgj@ysu.edu.cn (W.J.)
2   Mechanical and Electrical Engineering, Xinjiang Institute of Engineering, Urumqi 830023, China
3   School of Intelligent Systems Engineering, Sun Yat-sen University, Guangzhou 510275, China; yangsh235@mail.sysu.edu.cn
*   Correspondence: cgx@xjie.edu.cn; Tel.: +86-0991-7977195

Abstract: As the 'heart' of energy vehicles, the lithium-ion battery is in desperate need of precision improvement, green production, and cost reduction. To achieve this goal, the electro-hydraulic servo pump control system (EHSPCS) is applied to the lithium-ion battery pole rolling mill (LBPRM). However, this development can lead to limited dynamic performance and large power loss as a result of the EHSPCS unique volume direct-drive control mode. At present, how to solve this conflict has not been studied and how the EHSPCS component parameters influence the dynamic response, power loss, and economic performance is not clear. In this paper, a multi-objective optimization (MOO) model for the LBPRM-EHSPCS is proposed by comprehensively considering the dynamic, efficiency, and economic characteristics. Firstly, the evaluation model of the dynamic response, power loss, and cost is investigated. Then, the NSGA-II algorithm is introduced to address the Pareto front of the MOO model. Finally, the power loss and dynamic response of the LBPRM-EHSPCS before and after optimization are tested to validate the viability of the raised method. Results indicate that power loss is decreased by as much as 7.2% while steady-state precision is greatly improved after optimization. The proposed framework enhances the performance in lithium-ion battery manufacturing and can be applied to other kinds of hydraulic systems.

Keywords: lithium-ion battery pole rolling mill (LBPRM); electro-hydraulic servo pump control system (EHSPCS); optimum design; NSGA-II; dynamic characteristics; efficiency characteristics; economic characteristics

1. Introduction

Power lithium-ion batteries have remained the dominant power source for new energy vehicles due to their no memory influence, high specific energy, long cycle life, and lack of pollution [1–3]. These batteries are widely applied in various fields including portable electronics, electric vehicles, and renewable energy storage [4–6]. The safety and cruising range of the entire vehicle is primarily determined by the performance of the power lithium-ion battery. The positive and negative electrode piece crucial indicators, which include consistent thickness, compaction density, and strip strength, directly impact the battery's performance [7,8].

Long-term studies on battery electrodes have mostly examined the effects of active materials [9,10], formulations [11–13], and conductive agent selection [14–16] on battery electrochemical performance. Precision and efficiency for the pole plate rolling process are increasingly urgently needed as battery performance and safety requirements improve. The LBPRM typically presses the battery electrode to a predetermined thickness through the hydraulic automatic gauge control (HAGC) [17,18]. In the HAGC, electro-hydraulic servo valve (EHSV) control cylinder technology is frequently employed. By using a servo valve

to control the roll gap of the LBPRM, the battery pole piece may be formed accurately with excellent performance [19]. The EHSV automatic gauge control (EHSV-AGC) possesses the benefit of effective control performance. However, the device's complex architecture causes it to be poorly integrated and takes up a lot of room. Meanwhile, the throttling loss of the valve port is serious, which contributes to great energy dissipation. Moreover, the EHSV-AGC requires extremely clean oil (NAS 3-5), necessitating the use of an extra-precise filtration mechanism that raises the cost of installation.

The LBPRM-EHSPCS system was proposed to achieve the high-precision rolling of lithium battery electrodes to address the aforementioned technical deficiencies. With significant integration with hydraulic cylinders, servo motors, fixed-displacement pumps, and functional valve groups [20], the EHSPCS is a volumetric servo control module. It offers advantages including high efficiency, environmental friendliness, and great power-to-weight ratio [21]. The EHSPCS is widely applied in high-precision control fields such as flight control [22], wind variable propeller control [23], and hydraulic excavator arm drive systems [24]. The electro-mechanical-hydraulic coupling nonlinear mechanism [25,26], high-performance control strategies [27,28], and thermal power characteristics [29,30] are the key study areas of the EHSPCS.

The LBPRM-EHSPCS's installed cost, occupied space, and energy consumption ratio are all reduced when compared to EHSV control technology by roughly 30%, 80%, and 65%, respectively. Despite having these benefits, the LBPRM-EHSPCS's dynamic performance is constrained due to the high motor-pump inertia. Thermal power loss is also serious because of high integration [31]. Meanwhile, the economic characteristics of the LBPRM-EHSPCS are essentially taken into consideration to reduce installed costs. Consequently, the characteristics of dynamic, efficiency, and economy are crucial factors for evaluating the manifestation of the LBPRM-EHSPCS. However, as a multi-parameter, tightly coupled, and non-linear complicated system, these three elements frequently interact with one another and have a complex non-linear relationship with the design variables, which is a MOO problem. To maximize the system's complete performance, it is vital to think about how it determines it eclectically.

The NSGA-II, a MOO algorithm applicable for processing non-sequential, high-dimensional, and multi-polar numbers [32,33], is successful in many engineering fields. Concretely, a MOO model for the multi-scale textured slipper/swash plate interface using the NSGA-II was raised to improve the tribological properties and the efficiency of EHA pumps [34]. The characteristics of pressure relief and flame-retardation of an explosion-proof valve were optimized using the Kriging model and NSGA-II [35]. A novel approach to improve centrifugal pump performance for the pump head, pump efficiency, and power was proposed [36]. The K-shaped notches of the multi-way spool valve were optimized by CFD analysis, DAPM model, and NSGA-II algorithm [37]. Especially, the optimal matching of the dynamic characteristics and the thermal power loss for the hydraulic servo motor EHSPCS were studied. The NSGA-II algorithm showed better performance compared to the multi-objective particle swarm algorithm [38]. Consequently, the NSGA-II is operated to optimize design parameters for the LBPRM-EHSPCS in this paper. Meanwhile, the economic characteristics are significant for the broader application of the LBPRM-EHSPCS. However, the economic characteristics research is absent and only the thermal power loss of the servo motor is taken into consideration for research [38].

The relevant evaluation models of the valuable components are established in this study with a focus on the dynamic, efficient, and economic characteristics of the LBPRM-EHSPCS. The design parameters of the servo motor, fixed-displacement pump, and hydraulic cylinder of the LBPRM-EHSPCS are optimized to achieve efficient dynamic response, low power loss, and cost. The NSGA-II is adopted to obtain the Pareto front with good diversity. The optimization process in this paper is valuable for the optimization design of high-performance LBPRM-EHSPCS.

In the following sections, we first establish the mathematical model of the kinetic characteristics for the LBPRM-EHSPCS in Section 2. The MOO model is built and the

kinetic parameters are optimized in Section 3. In addition, the performances including dynamic and efficiency characteristics of the LBPRM-EHSPCS before and after optimization are compared in Section 4.

2. Kinetic Characteristics of the LBPRM-EHSPCS

The LBPRM-EHSPCS belongs to a volumetric servo control system made up of a drive unit (permanent magnet synchronous servo motor), power unit (two-way quantitative plunger pump), execution unit (hydraulic cylinder), control unit (controller and servo driver), and other hydraulic accessories (check valve, safety valve, accumulator, and so on). The working principle of the LBPRM-EHSPCS is shown the Figure 1. The LBPM-EHSPCS adopts a keyless connection. The oil is supplied by the fixed-displacement pump via the servo motor by coaxial direct drive. The oil inlet and outlet of the fixed-displacement pump are connected immediately to two loading ports. The relief valve serves as overload prevention, and the accumulator fulfills the function of oil storage and supplementation in place of the conventional oil tank. The controller gathers the location, pressure, and other feedback from the system using a variety of sensors. As a result, the servo driver receives input commands from the host computer to control the LBPM-EHSPCS with high-accuracy closed-loop feedback.
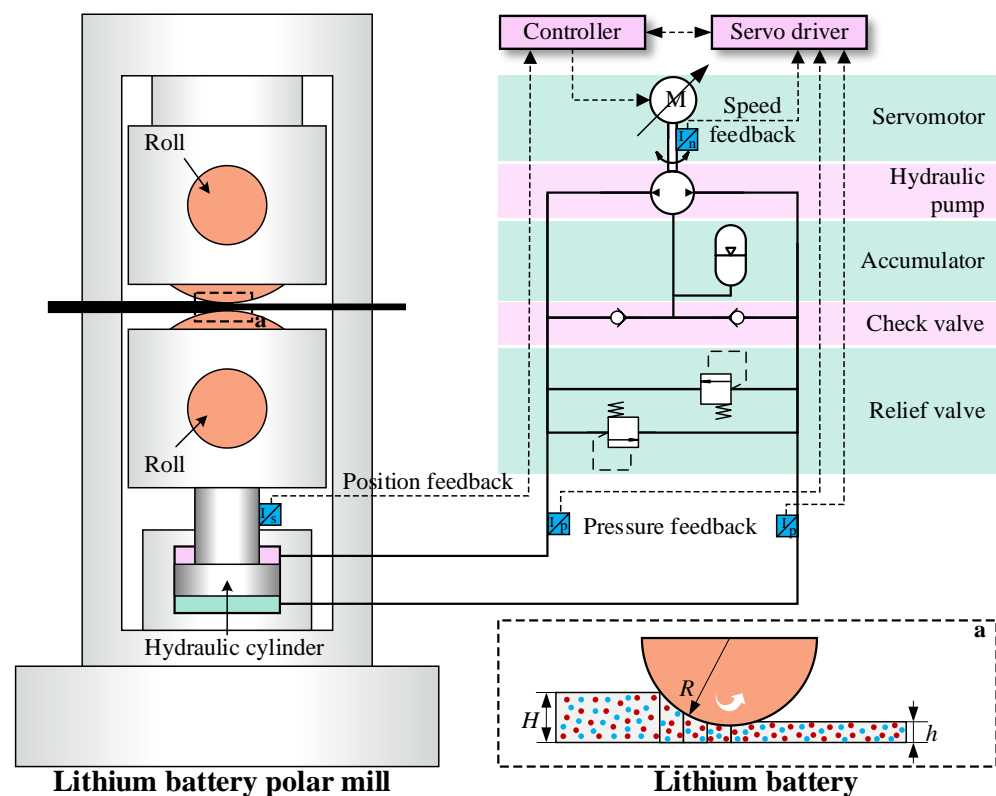

Figure 1. Working principle of the LBPRM-EHSPCS.

The outstanding working efficiency, dynamic characteristics, and economic performance of the LBPRM-EHSPCS are essential elements related to the adoption and promotion of this technology in engineering applications. Consequently, it is assumed that the optimization goals in this section will be efficiency, dynamics, and economics. These three characteristics are examined from the perspectives of power loss, frequency response, and actual market, respectively. Additionally, the key kinetic parameters affecting the performance are found.

2.1. Dynamic Characteristics

The good dynamic characteristics of the LBPRM-EHSPCS are conducive to ensuring the system is stable, which can deliver a foundation for improving the existing system. The dynamic characteristics are analyzed from the frequency response of the LBPRM-EHSPCS in this part. Especially, the sinusoidal signal is used for tracking to analyze the performance of the dynamic characteristic. It is assumed that the given sinusoidal signal amplitude is B and the frequency is f. The displacement curve of the hydraulic cylinder is characterized by Equation (1):

$$x_L = B \sin(2\pi f t), \tag{1}$$

where t is the hydraulic cylinder displacement time.

Furthermore, the operating speed of the hydraulic cylinder is shown in Equation (2):

$$v_L = 2\pi f \gamma B \cos(2\pi f t), \tag{2}$$

where γ is the attenuated percentage of B.

The hydraulic cylinder load force at zero loads can be derived as Equation (3) from Equations (1) and (2):

$$F_L = M a_L = M(2\pi f)^2 \gamma B \sin(2\pi f t), \tag{3}$$

where F_L is the hydraulic cylinder load force, M is the load, and a_L is the acceleration.

Thus, the required power of the hydraulic cylinder P_L is:

$$P_L = F_L v_L = \frac{1}{2}(2\pi f)^3 M \gamma^2 B^2 \sin(4\pi f t), \tag{4}$$

where v_L is the velocity of the hydraulic cylinder.

The required flow rate Q_L is expressed in Equation (5):

$$Q_L = v_L A_L = 2\pi f A_L B \cos(2\pi f t), \tag{5}$$

where A_L is the hydraulic cylinder working area. Without considering the fixed-displacement pump leakage, the pump's theoretical output flow Q should be described as Equation (6):

$$Q = D_p w, \tag{6}$$

where D_p is the fixed-displacement pump displacement, w is the servo motor angular velocity.

The angular velocity w and speed n of the servo motor pump are achieved as Equations (7) and (8):

$$w = \frac{Q}{D_p} = \frac{2\pi f A_L \gamma B}{D_p} \cos(2\pi f t), \tag{7}$$

$$n = \frac{60w}{2\pi} = \frac{60 f A_L \gamma B}{D_p} \cos(2\pi f t). \tag{8}$$

In the case of zero loads of the system, the servo motor angular acceleration a and torque required T_e can be expressed as Equations (9) and (10):

$$\alpha = \frac{(2\pi f)^2 A_L \gamma B}{D_p} \sin(2\pi f t), \tag{9}$$

$$T_e = J_{mp}\alpha = \frac{J_{mp}(2\pi f)^2 A_L \gamma B}{D_p} \sin(2\pi f t), \tag{10}$$

where J_{mp} is the motor pump group rotor inertia.

Furthermore, the motor load curve can be calculated as Equation (11):

$$\left[\frac{T_e D_p}{J_{mp}(2\pi f)^2 A_L \gamma B}\right]^2 + \left(\frac{n D_p}{60 f A_L \gamma B}\right)^2 = 1. \tag{11}$$

The required power P of the motor is shown in Equation (12):

$$P = T_e w = \frac{J_{mp}(2\pi f)^3 (A_L B)^2 \gamma}{2 D_p}\sin(4\pi ft). \tag{12}$$

The hydraulic cylinder output force could be converted to the moment of the motor-pump output shaft such as in Equation (13):

$$T_L w = F_L v_L, \tag{13}$$

The equivalent load torque T_L can be calculated as Equation (14):

$$T_L = \frac{D_p}{A_L}(2\pi f)^2 M \gamma B \sin(2\pi ft). \tag{14}$$

Thus, the motor torque can be described as Equation (15):

$$T_e = J_{mp}\alpha + T_L = \left(\frac{m D_p^2 + J_{mp} A_L^2}{A_L D_p}\right)(2\pi f)^2 \gamma B \sin(2\pi ft). \tag{15}$$

The dynamic characteristics of the system are shown in Equation (16):

$$f = \frac{\sqrt{\frac{T_{max} A_L D_p}{B\gamma(M D_p^2 + J_{mp} A_L^2)}}}{2\pi} = \frac{\sqrt{\frac{T_{max}}{B\gamma\left(M \frac{D_p}{A_L} + J_{mp}\frac{A_L}{D_p}\right)}}}{2\pi} \quad (A_L \neq 0, D_p \neq 0). \tag{16}$$

According to Equation (16), it can be inferred that the factors influencing the dynamic characteristics are the servo motor maximum torque, the moment of inertia of the motor pump set, the fixed-displacement pump displacement, the hydraulic cylinder area, and the total mass of the piston rod and load; but this factor is not considered in this paper due to the time-varying load.

The Matlab/Simulink simulation model is built to investigate the dynamic characteristics of the EHSPCS according to Equation (16). Meanwhile, the four factors of the dynamic characteristics are simulated and shown in Figure 2. In Figure 2, the abscissa represents the fixed period while the ordinate represents the response time. The percentage in the figure means the relative error (the ratio of the difference to the larger value). With the increase of servo motor torque, fixed-displacement pump displacement, a moment of inertia, and hydraulic cylinder working area, the system response time is shortened to varying degrees. Among them, the moment of inertia has the least impact on the response time with a maximum relative error of 9%, and the fixed-displacement pump displacement possesses the greatest impact with a minimum relative error of 55.1%. Consequently, the factors of servo motor torque, fixed-displacement pump displacement, and hydraulic cylinder working area are taken as the key kinetic parameters of the LBPRM-EHSPCS.
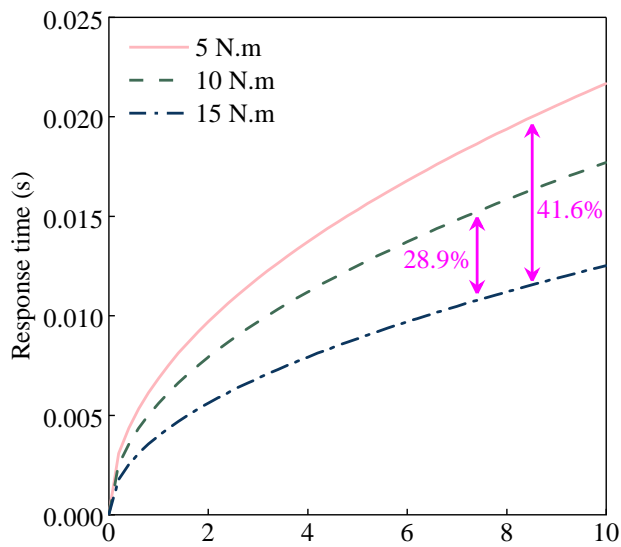
(**a**) Servo motor torque
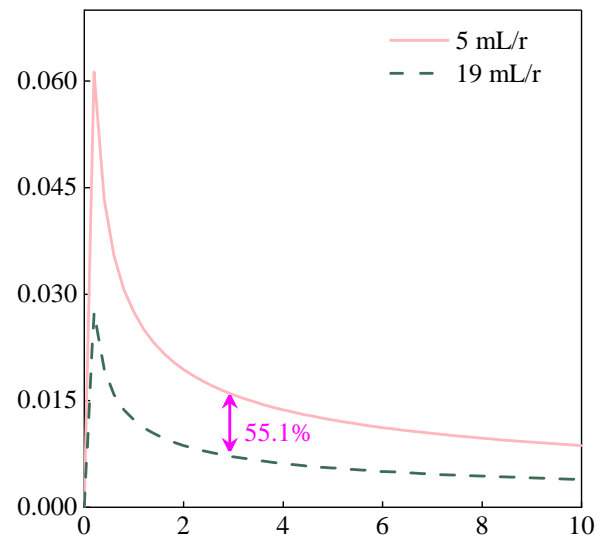
(**b**) Fixed-displacement pump displacement
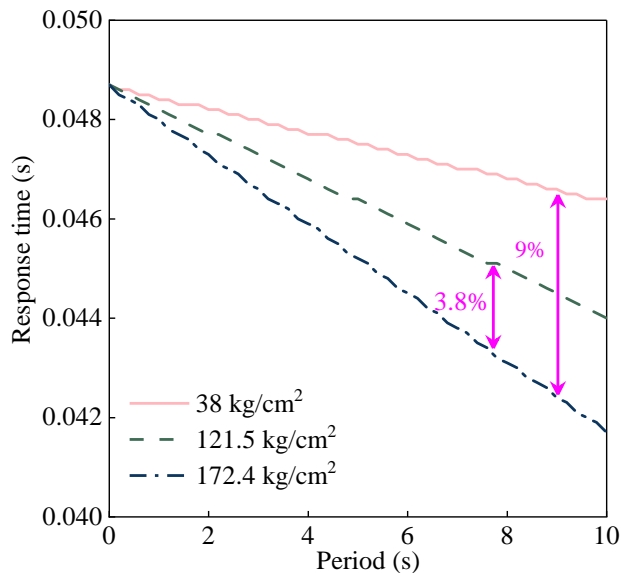
(**c**) Moment of inertia
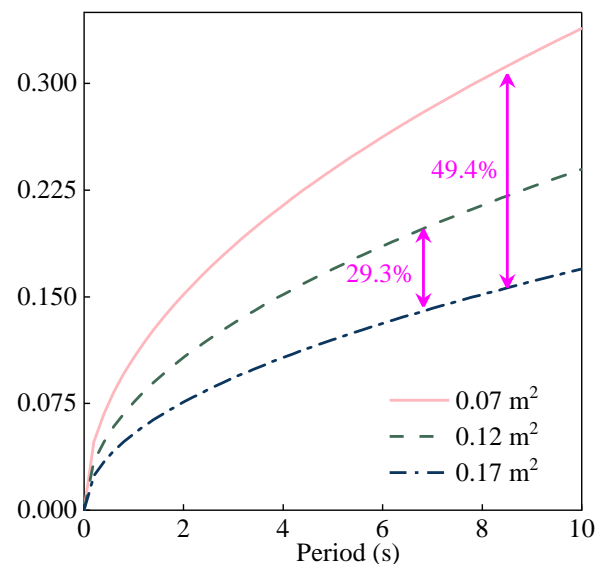
(**d**) hydraulic cylinder working area

Figure 2. Kinetic characteristics of various kinetic parameters.

2.2. Efficiency Characteristics

Every component has its inherent energy losses, such as the loss of heat transfer and mechanical friction caused by the servo motor, the volume loss caused by the fixed-displacement pump due to its volumetric efficiency and the loss caused by mechanical friction, and the loss caused by friction and leakage of the hydraulic cylinder. The schematic diagram of energy flow loss is shown in Figure 3.

Figure 3. Schematic diagram of system energy flow loss.

2.2.1. Servo Motor Power Loss

The loss of the servo motor could be attributed to various factors including stator iron consumption, winding copper consumption, and mechanical wear.

(1) Stator iron loss

The energy loss of the stator core can be expressed as Equation (17):
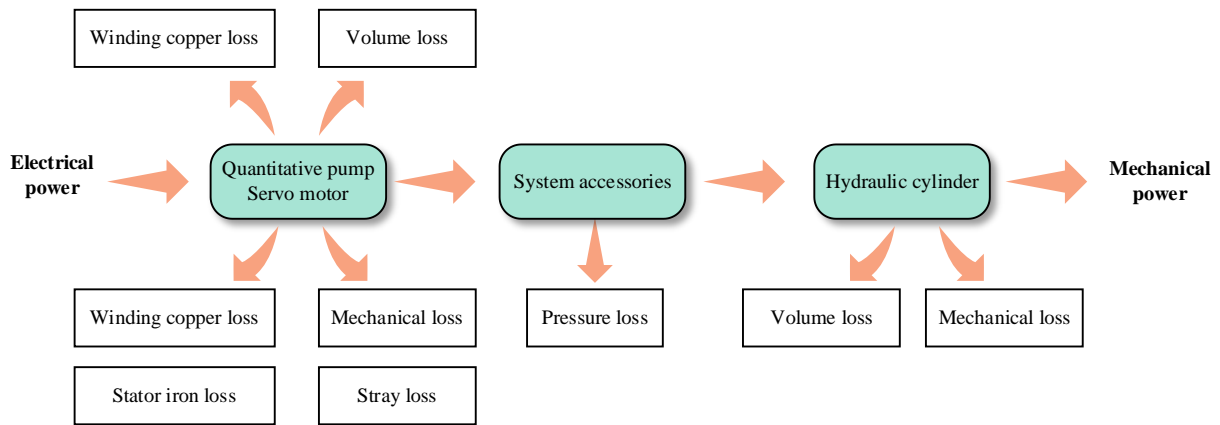
$$P_{\mathrm{Fe}} = P_{\mathrm{c}} + P_{\mathrm{h}} + P_{\mathrm{e}} = k_{\mathrm{c}} f_1^2 B_{\mathrm{m}1}^2 + k_{\mathrm{h}} f_1^2 B_{\mathrm{m}1}^{\beta_1} + k_{\mathrm{e}} f_1^{1.5} B_{\mathrm{m}1}^{1.5}, \tag{17}$$

where P_{Fe} is the stator iron loss, P_{c} is the eddy current loss, P_{h} is the hysteresis loss, P_{e} is the additional loss, k_{c} is the eddy current loss coefficient, f_1 is the alternating magnetic field frequency, $B_{\mathrm{m}1}$ is the magnetic density value, k_{h} is the hysteresis loss coefficient, β_1 is the Steinmetz coefficient, k_{e} is the additional loss coefficient.

(2) Winding copper loss

Winding copper loss refers to the power loss as the effect of resistance when immediately flows through the winding coil. According to Joule's law, the winding copper loss could be described as Equation (18):

$$P_{\mathrm{Cu}} = mI^2 R, \tag{18}$$

where P_{Cu} is the loss of the winding copper, m is the motor phase, $m = 3$, I is the effective value of motor phase current, and R is the resistance value of each phase.

(3) Mechanical power loss

Mechanical losses mainly include bearing friction losses and rotor friction losses such as Equation (19):

$$P_{\mathrm{m}} = k_{\mathrm{r}} C_{\mathrm{m}} \rho w^3 r^4 l, \tag{19}$$

where P_{m} is the mechanical power loss, k_{r} is the rotor surface roughness, ρ is gas density, w is the rotor angular velocity, C_{m} is the coefficient of friction, r is the rotor radius, and l is the rotor axial length.

In all, the total power loss of the servo motor can be expressed as Equation (20):

$$P_{\mathrm{loss}}^{\mathrm{motor}} = k_{\mathrm{c}} f^2 B_{\mathrm{m}1}^2 + k_{\mathrm{h}} f^2 B_{\mathrm{m}1}^{\beta_1} + k_{\mathrm{e}} f^{1.5} B_{\mathrm{m}1}^{1.5} + mI^2 R + k_{\mathrm{r}} C_{\mathrm{m}} \rho w^3 r^4 l. \tag{20}$$

2.2.2. Fixed-Displacement Pump Power Loss

The fixed-displacement radial piston pump energy loss is composed of volume loss and mechanical friction loss. Concretely, the power loss can be divided into the leakage of heat and the frictional heat. These two power losses mainly occur in the plunger pair, sliding shoe pair, and distribution pair of the radial piston pump. The power flow for the radial piston pump is shown in Figure 4.
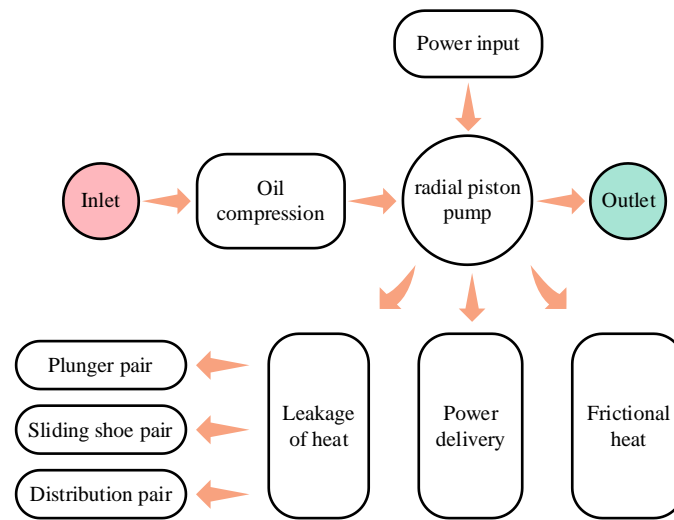
Figure 4. Schematic diagram of radial piston pump power flow.

(1) Volume loss

The plunger side leakage is caused by the combination of the shear and differential pressure flow. The shear flow is the relative movement of the plunger and the inside of the cylinder block. The differential pressure flow is the difference between the pump pressure and the return pressure. The release between the single plunger and the cylinder block is shown in Equation (21):

$$Q_{L1} = \frac{\pi d_p \delta_p{}^3 \Delta p_1}{12\mu L_p}\left(1 + 1.5\varepsilon^2\right), \tag{21}$$

where Q_{L1} is the release between the plunger and the cylinder block, d_p is the plunger diameter, δ_p is the gap between the plunger and the inner wall of the cylinder bore, Δp_1 is the pressure drop of the piston pump, m is the oil dynamic viscosity, L_p is the length of contact between the plunger and the cylinder bore, ε is the eccentricity, $\varepsilon = e/\delta_p$, e is the eccentric amount.

The shoe pair may leak as a result of the differential pressure flow, causing oil leakage. Therefore, the amount of leakage generated between a single shoe and the stator void can be calculated as Equation (22):

$$Q_{L2} = \frac{\pi h^3 (p_r - p_0)}{6\mu \ln \frac{r_2}{r_1}}, \tag{22}$$

where Q_{L2} is the leakage between the slip shoe and the stator, h is the thickness of the oil film between the stator and the shoe, r_1 is the inner radius of the shoe sealing belt, and r_2 is the outer radius of the shoe sealing belt.

The leakage of the distribution pair of the plunger pump is caused by the gap between the distribution shaft and the rotor. The leakage amount between the distribution shaft and the rotor could be described as Equation (23):

$$Q_{L3} = \frac{f_v r_v \delta_v{}^3}{12\mu L_v}, \tag{23}$$

where Q_{L3} is the leakage of the distribution shaft and rotor, f_v is the leaking packet corners, r_v is the distribution shaft radius, δ_v is the clearance between the plunger and the rotor, and L_v is the contact length.

(2) Mechanical loss

(a) Plunger pair friction loss

According to the operating state of the plunger cavity, it can be divided into oil suction chamber, pressure oil chamber, and closed cavity. The frictional power loss of each plunger pair can be described as Equation (24):

$$P_{f1} = F_{f1}v_L = \left(\mu \frac{v_p}{\delta_1} \pi d_p L_p + \frac{\pi d_p \delta_1}{2} \Delta p_1 \right) v_L, \tag{24}$$

where P_{f1} is the plunger pair friction loses power, F_{f1} is the plunger pair friction, d_p is the plunger diameter, δ_1 is the clearance between the plunger and the cylinder block, and L_p is the plunger width.

(b) Slip shoe pair friction loss

A thin and balanced annular oil film is created between the sealing tape of the shoe and the stator and the frictional power loss generated by this oil film can be expressed as Equation (25):

$$P_{f2} = T_{f2}w_2, \tag{25}$$

where P_{f2} is the sliding shoe pair friction power loss, T_{f2} is the torque at the sliding shoe, and w_2 is the stator speed.

(c) Distribution pair friction loss

The oil film formed between the distribution shaft and the rotor is approximately a parallel annular disc-type gap flow, so the frictional power loss can be described as Equation (26):

$$P_{f3} = T_{f3}w_3, \tag{26}$$

where P_{f3} is the distribution pair friction loses power, T_{f3} is the distribution shaft torque, and w_3 is the rotor speed.

In summary, the total power loss of the fixed-displacement pump could be expressed as the sum of the volume loss and the mechanical friction loss can be expressed in Equation (27):

$$P_{loss}^{pump} = \left[\sum_{i=1}^{N} (Q_{L1} + Q_{L2}) + Q_{L3} \right] \Delta p_1 + \left[\sum_{i=1}^{N} (P_{f1} + P_{f2}) + P_{f3} \right], \tag{27}$$

where N is the number of plunger pump plungers.

2.2.3. Hydraulic Cylinder Power Loss

Hydraulic cylinder power loss is divided into leakage loss and mechanical friction loss. The hydraulic cylinder leakage amount could be shown as Equation (28):

$$Q_{Lc} = \pi d_c h_c \left(\frac{\Delta p_2 h_c^2}{12\mu l_c} \pm \frac{v_c}{2} \right), \tag{28}$$

where Δp_2 is the pressure drop of the cylinder's two cavities, v_c is the piston rod speed.

Hydraulic cylinders are affected by the oil film shear during piston movement, which leads to the formation of friction forces. The frictional force experienced by the piston can be described as Equation (29):

$$F_{fc} = \tau S_c = \pi d_c \left(\frac{l_c \mu v_c}{h_c} - \frac{\Delta p_2 h_c}{2} \right). \tag{29}$$

Based on the above analysis, the overall power loss of the hydraulic cylinder is expressed in Equation (30):

$$P_c = \pi d_c \left[h_c \left(\frac{\Delta p_2 h_c^2}{12\mu l_c} \pm \frac{v_c}{2} \right) \Delta p_2 + \left(\frac{l_c \mu v_c}{h_c} - \frac{\Delta p_2 h_c}{2} \right) v_c \right]. \tag{30}$$

According to the above analysis of the power loss for the servo motor, fixed-displacement pump, and hydraulic cylinder, the system's total power loss is approximated. The power loss of the LBPRM-EHSPCS is shown in Figure 5.
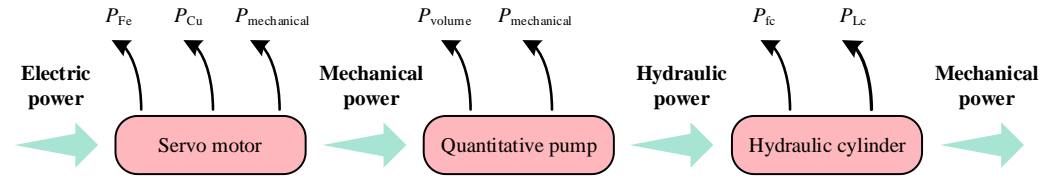

Figure 5. The power loss of various components for the LBPRM-EHSPCS.

For facilitating the general analysis of the system power loss, the kinetic parameters of each component need to be converted through the intermediate variable relationship such as Equation (31):

$$
\begin{cases}
F_q = A_L P_L \\
\dot{x}_p = \dfrac{D_p w_p}{A_L} \\
T_e = D_p P_L
\end{cases} .
\tag{31}
$$

According to the servo motor power loss analysis, it can be obtained that the servo motor efficiency is characterized by Equation (32):

$$
\eta_m = \frac{P_0 - P_{loss}^{motor}}{P_0},
\tag{32}
$$

where P_0 is the input power of the servo motor shaft, $P_0 = \sqrt{3}UI\cos\phi$, U is the input voltage of the motor, I is the input current of the motor, $\cos\phi$ is the power factor of the motor, $\cos\phi = 0.85$.

The servo motor torque is shown in Equation (33):

$$
T_e = k_t I,
\tag{33}
$$

where k_t is the torque constant.

The association between the motor speed and frequency is expressed as Equation (34):

$$
n = \frac{60f}{p}, p = 3,
\tag{34}
$$

where n is the motor speed.

In summary, the efficiency of the servo motor can be derived as Equation (35):

$$
\eta_m = \frac{\sqrt{3}UT_e\cos\phi - k_t\left(k_c\left(\frac{np}{60}\right)^2 B_{m1}^2 + k_h\left(\frac{np}{60}\right)B_{m1}^{\beta1} + k_e\left(\frac{np}{60}\right)^{1.5}B_{m1}^{1.5} + n\left(\frac{T_e}{k_t}\right)^2 R + k_r C_m \rho \omega^3 r^4 l\right)}{\sqrt{3}UT_e\cos\phi}.
\tag{35}
$$

From Equation (36), it can be concluded that the motor efficiency is related to the torque and speed. The greater the torque and speed, the more the motor loses.

The fixed-displacement pump volumetric efficiency is expressed in Equation (36):

$$
\eta_v = \frac{Q - \Delta Q}{Q} \times 100\%.
\tag{36}
$$

The fixed-displacement pump's mechanical efficiency is shown in Equation (37):

$$
\eta_{mp} = \frac{P - \Delta P}{P} \times 100\%.
\tag{37}
$$

Furthermore, the fixed-displacement pump's total efficiency can be characterized as Equation (38):

$$\eta_{\mathrm{P}} = \eta_{\mathrm{v}}\eta_{\mathrm{mp}},\tag{38}$$

where η_{v} is the volumetric efficiency, η_{m} is the mechanical efficiency, and η_{P} is the total efficiency of the metered pump.

The fixed-displacement pump' total efficiency can be expressed as Equation (39):

$$\eta_{\mathrm{P}} = \frac{n \cdot D_{\mathrm{P}} - 1000\Delta p \left(\frac{\pi d_{\mathrm{P}}\delta_{\mathrm{P}}^3}{12\mu L_{\mathrm{P}}}(1 + 1.5\varepsilon^2) + \frac{\pi h^3}{6\mu \ln \frac{r_2}{r_1}} + \frac{f_{\mathrm{v}}r_{\mathrm{v}}\delta_{\mathrm{v}}^3}{12\mu L_{\mathrm{v}}} \right)}{n \cdot D_{\mathrm{P}}} \cdot \frac{1000PQ}{\Delta p D_{\mathrm{P}}n}.\tag{39}$$

Based on the above research, it can be concluded that the loss of the fixed-displacement pump is related to the speed and pressure.

According to the hydraulic cylinder power loss analysis, the hydraulic cylinder efficiency can be expressed as Equation (40):

$$\eta_{\mathrm{hc}} = \frac{P_{\mathrm{m}} - P_{\mathrm{c}}}{P_{\mathrm{m}}} \times 100\% = \frac{P_{\mathrm{m}} - \pi d_{\mathrm{c}} \left[h_{\mathrm{c}}\left(\frac{\Delta p_2 \cdot h_{\mathrm{c}}^2}{12\mu l_{\mathrm{c}}} \pm \frac{v_{\mathrm{c}}}{2} \right)\Delta p_2 + \left(\frac{l_{\mathrm{c}}\mu v_{\mathrm{c}}}{h_{\mathrm{c}}} - \frac{\Delta p_2 h_{\mathrm{c}}}{2} \right)v_{\mathrm{c}} \right]}{P_{\mathrm{m}}}.\tag{40}$$

where P_{m} and P_{c} are the hydraulic cylinder power of the inlet and outlet.

The analysis above indicates that the hydraulic cylinder working area, or diameter of the piston rod, is proportional to the hydraulic cylinder efficiency. Particularly, the hydraulic cylinder loses more pressure the larger the working surface.

In all, the overall efficiency of the LBPRM-EHSPCS can be expressed as Equation (41):

$$\eta = \eta_{\mathrm{m}} \cdot \eta_{\mathrm{p}} \cdot \eta_{\mathrm{hc}},\tag{41}$$

where η is the system total efficiency, η_{m} is the servo motor total efficiency, η_{p} is the fixed-displacement pump total efficiency, and η_{hc} is the hydraulic cylinder total efficiency.

2.3. Economic Characteristics

LBPRM-EHSPCS is typically configured as the equipment's maximum power demand because it is an important power output device. The majority of the time, the operational conditions of the equipment prevent it from running at maximum capacity, which results in significant resource consumption. Meanwhile, if the low-power operation is performed for an extended period, the rolling precision will decline. It is challenging to balance cost and energy use, according to prior engineering experience. From the standpoint of the actual labor demand, the economy must be taken into account.

The economic prediction model of the main components requires to be built to check the economic budget of the LBPRM-EHSPCS in the preliminary design stage. The LBPRM-EHSPCS is chiefly constituted of software and hardware. The software mainly includes an upper computer, controller, drive, and other control components. A fixed-displacement pump, servo motor, hydraulic cylinder, and other hydraulic accessories make up the majority of the hardware element.

The hardware part of the LBPRM-EHSPCS is paid more attention to in this paper, and its economic formula can be expressed as Equation (42):

$$R_{\mathrm{hard}} = R_{\mathrm{motor}} + R_{\mathrm{pump}} + R_{\mathrm{cylinder}},\tag{42}$$

where R_{motor}, R_{pump}, and R_{cylinder} are the costs of the servo motor, fixed-displacement pump, and hydraulic cylinder, respectively.

2.3.1. Servo Motor Cost

The permanent magnet synchronous motor (PMSM) has excellent efficiency, robust overload capacity, high operating dependability, and huge starting torque. Because the

torque has a significant impact on the LBPRM-EHSPCS' performance, PMSMs are typically used in this system. Consequently, Equation (43) can be used to represent the economic curve of the motor:

$$R_{\mathrm{motor}} = a_1 T_{\mathrm{e}}{}^2 + a_2 T_{\mathrm{e}} + a_3,\tag{43}$$

where a_1, a_2, and a_3 are curve-fitting parameters.

Especially, the reference high-speed servo motors of this study are mainly derived from the company of INOVANCE, Physis, and Delta. The speed range of the motor is 0–3000 r/min. The prediction curve can be obtained by data fitting (see Figure 6a). The curve-fitting parameters are that $a_1 = 0.00615$, $a_2 = 37.51$, and $a_3 = 3232.88$.
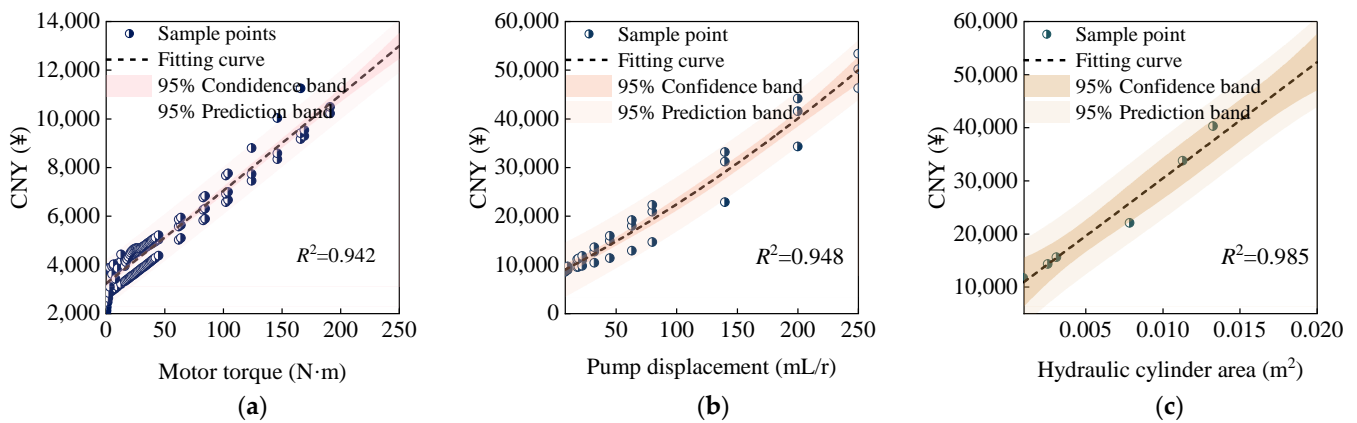

Figure 6. Prediction curve of economic characteristics: (**a**) Servo motor; (**b**) Fixed-displacement pump; (**c**) Hydraulic cylinder.

2.3.2. Fixed-Displacement Pump Cost

The key parameters of fixed-displacement pumps are displacement and pressure resistance. Therefore, it can be assumed that the economic curve of the fixed-displacement pump is shown in Equation (44):

$$R_{\mathrm{pump}} = b_1 D_{\mathrm{p}}{}^2 + b_2 D_{\mathrm{p}} + b_3,\tag{44}$$

where b_1, b_2, and b_3 are fitting parameters.

The sample parameters of the fixed-displacement pump are collected from the companies of MOOG, Rexroth, and Kawasaki. The fitted curve is shown in Figure 6b. The curve-fitting parameters are that $b_1 = 0.15$, $b_2 = 129.36$, and $b_3 = 7939.33$.

2.3.3. Hydraulic Cylinder Cost

It can be considered that the hydraulic cylinder's working area is its most crucial component and that the hydraulic cylinder's economic curve can be represented by Equation (45):

$$R_{\mathrm{cylinder}} = c_1 A_{\mathrm{L}}{}^2 + c_2 A_{\mathrm{L}} + c_3,\tag{45}$$

where c_1, c_2, and c_3 are fitting parameters.

The fitted curve is shown in Figure 6c. The curve-fitting parameters are that $c_1 = 1.14 \times 10^6$, $c_2 = 2.16 \times 10^6$, and $c_3 = 8744.78$.

According to the research above, the servo motor output torque, the displacement of the fixed-displacement pump, and the working area of the hydraulic cylinder are the three most crucial factors affecting the system's economic performance. In light of this, adjusting the corresponding kinetic parameters can enhance the system's economic performance.

3. Optimization Design Using NSGA-II

As the kinetic characteristics analysis of the LBPRM-EHSPCS, the optimization of the performance indexes is conducted in this section. The NSGA-II is introduced to seek the optimal design parameters of the LBPRM-EHSPCS.

3.1. MOO Model

The MOO model including objective functions, decision variables, and constraint conditions is developed in this part for optimization.

3.1.1. Objective Functions

The objective of optimization is to guarantee a quick dynamic response and weak power loss and cost. Consequently, the efficiency, frequency, and economic values are selected as the objective functions such as Equation (46), to achieve the goals of the highest efficiency, best dynamic characteristics, and best economic performance:

$$\begin{cases} y_1 = 1 - \eta \\ y_2 = \frac{1}{f} \\ y_3 = R_{\text{hard}} \end{cases}. \tag{46}$$

3.1.2. Decision Variables

It is noteworthy that the servo motor torque, the fixed-displacement pump displacement, and the hydraulic cylinder working area from the preceding study are directly related to the system dynamic, efficiency, and economic performance. The choice variables (Equation (47)) are the hydraulic cylinder working area, fixed-displacement pump displacement, and servo motor working torque to achieve the best matching of system characteristics:

$$x = \left[T_e, D_p, A_L \right]^{\text{T}}. \tag{47}$$

3.1.3. Constraint Condition

Range constraints, ratio constraints, and volume limitations make up the majority of the restrictions for solving MOO issues. Of these, the range constraint requires that the variables used to make the decisions change within a reasonable range. To guarantee the rationality and viability of the decision variables, the variables are constrained as Equation (48) by the actual production conditions:

$$\begin{cases} 4.4 \leq T_e \leq 110 \ (\text{N} \cdot \text{m}) \\ 5 \leq D_p \leq 19 \ (\text{mL/r}) \\ 0.07 \leq A_L \leq 0.17 \ (\text{m}^2) \end{cases}. \tag{48}$$

In conclusion, the MOO problem can be described as Equation (49):

$$\begin{aligned} find \ x &= \left[T_e, D_p, A_L \right]^{\text{T}} \\ \begin{cases} \min\left\{ 1 - \eta \left(T_e, D_p, A_L \right), \frac{1}{f} \left(T_e, D_p, A_L \right), R_{\text{hard}} \left(T_e, D_p, A_L \right) \right\} \\ s.t. \ 4.4 \leq T_e \leq 110 \ (\text{N} \cdot \text{m}) \\ \quad 5 \leq D_p \leq 19 \ (\text{mL/r}) \\ \quad 0.07 \leq A_L \leq 0.17 \ (\text{m}^2) \end{cases} \end{aligned}. \tag{49}$$

3.2. MOO Using NSGA-II

The optimization of decision variables is carried out to seek the greatest dynamic response, minimum power loss, and cost of the LBPRM-EHSPCS in this part. NSGA-II is a fast nondominated sorting-based evaluation method that uses an elitism strategy and a crowding comparison technique in the population to boost calculation speed and precision, eventually collapsing to the Pareto-optimal set [32]. Following that, the decision-

maker can choose an optimal solution from the Pareto-optimal solution graph that satisfies the subjective design preferences. The process of optimization using NSGA-II for the LBPRM-EHSPCS is shown in Figure 7, and the basic steps of NSGA-II are as follows.

i. Initialize a random population of P_t ($t = 0$) with size M. The fitness value of every individual is calculated.

ii. Fast non-dominant ranking of the sample population is performed. The crowding distance of individuals is calculated, and the calculation method is expressed as Equation (50):

$$d_i = \sum_{j=1}^{k} \left| \frac{f_j^{i+1} - f_j^{i-1}}{f_j^{\max} - f_j^{\min}} \right|, \tag{50}$$

where d_i is the crowding distance of individuals, k represents the objective function number, f_j^{i+1} and shows the objective function j of individuals $i + 1$ and $i - 1$, $f_j^{\max}$ and $f_j^{\min}$ is the maximum and minimum values of objective function j.

iii. The subsample population Q_t ($t = 0$) is achieved through selection, crossover, and mutation.

iv. The sample population R_t with size $2M$ is achieved by combining P_t and Q_t and then ranked to a non-dominant solution set. Afterward, every individual crowding distance is calculated.

v. A new sample population P_{t+1} is obtained by choosing the optimal N individuals.

vi. A new subsample population Q_{t+1} is achieved by selection, crossover, and mutation towards P_{t+1}.

vii. The algorithm will circulate from step iv to vi till the maximum circulation number is achieved.
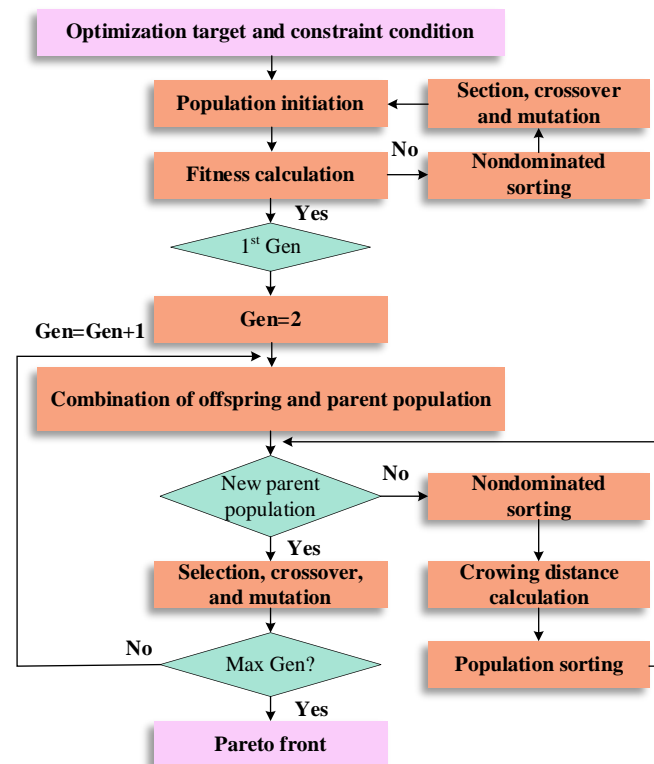

Figure 7. The process optimization using NSGA-II for the LBPRM-EHSPCS.

In this instance, 100 arbitrary random sets of the three fundamental decision variables will comprise the initial populations of NSGA-II. The dynamic, efficiency, and economic

objective function models are used in the NSGA-II adaptation calculation. The population of 100 is the starting point for the generation evolution, with a 0.1 mutation probability and a 0.9 crossover probability. In addition, 1000 evolution iterations are the maximum number that may be used to determine the ideal parameter settings for three typical choice variables and the associated objective functions.

The index of hypervolume (HV) and spacing are chosen during the optimal process to examine the Pareto front's algorithm efficiency and variation [39]. HV is a thorough assessment of the diversity and convergence of the solution group. A higher HV value indicates a more logical solution group. Spacing is used in NSGA-II to measure the dispersion of non-dominated solutions. A smaller spacing value indicates a better diversity and distribution of non-dominated solutions. Besides, spacing is more efficient for measuring MOO questions. The state of the NSGA-II optimal process is expressed in Figure 8. The Pareto-optimal group in this NSGA-II example has good potential for spread and diversification, with 0.86 HV and 0.006 spacing value. It has converged at 200 iterations of evolution. The Pareto-optimal set from the 1000th generation has been utilized in the present research due to its superior diversity and spread capability.
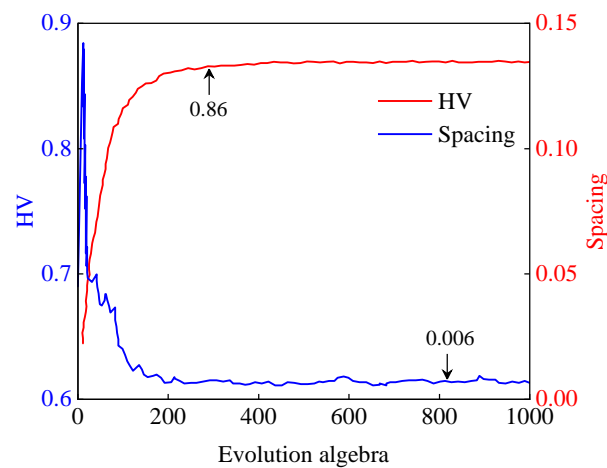

Figure 8. HV and spacing status.

4. Results and Discussion

4.1. Optimization Results

Under the given range limits, MOO seeks to maximize dynamic response while minimizing power loss and expense. Figure 9 depicts the trade-off between the Pareto solutions for the three objective functions. The MOO model suggested in this work achieves 100 groups of non-dominated solutions. The scope of the dynamic period (s) is [0.2, 1.2], the $1 - \eta$ is [42%, 56%], and the cost (¥) is [21,000, 26,000] in the Pareto hyperplane. It should be highlighted that simultaneously optimizing these three target functions is challenging. This allows for the "optimal solution" to be chosen by the system's actual operating circumstances. If designers give little thought to cost, Point A might be the best option. While point C has the lowest cost, its dynamic reactivity and efficiency are subpar. Point B is regarded as the optimal solution to balance these three optimization variables because it has a relatively quick dynamic response and low power loss and cost.
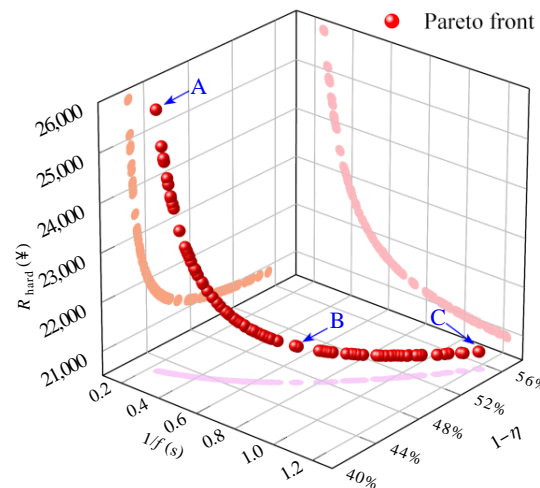
Figure 9. Pareto front from the NSGA-II optimization. Point A (0.25, 42.62%, 25,781), Point B (0.73, 46.91%, 21,239), and Point C (1.22, 55.34%, 20,860) are all points in the Pareto front.

Figure 10 represents the dispersion of every decision variable in the Pareto solutions. Concretely, the electromagnetic torque T_e in the Pareto frontier is mainly concentrated around 8.25 N·m and gradually decreases (Figure 10a). The hydraulic pump displacement value can be shown in Figure 10b to be mostly dispersed between 5.73 mL/r and 5.79 mL/r, with the sparsest portions spreading at both ends of the range of values. Additionally, between 0.145 and 0.149 m^2, the hydraulic cylinder working area A_L value is equally distributed (Figure 10c).
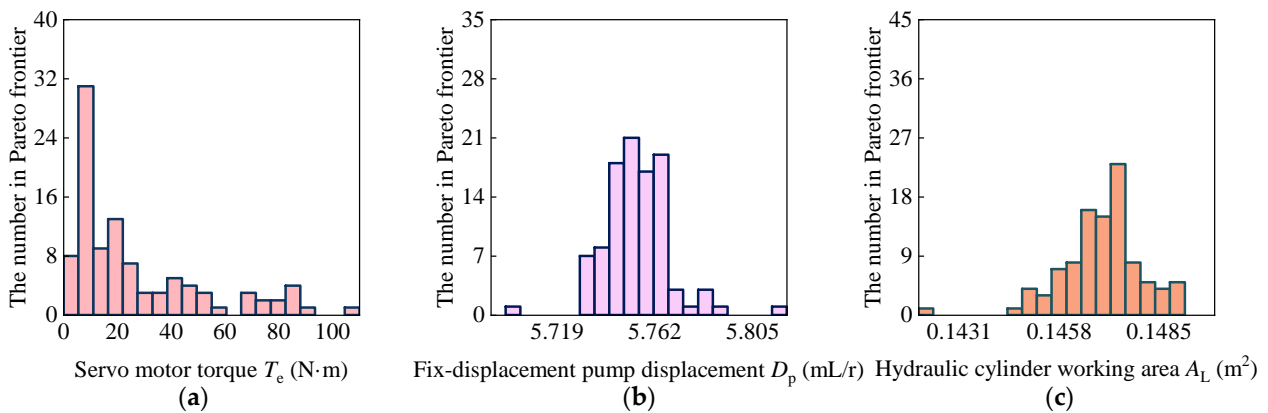

Figure 10. Pareto solutions of optimization for the LBPRM-EHSPCS: (**a**) Servo motor torque; (**b**) Fixed-displacement pump displacement; (**c**) Hydraulic cylinder working area.

4.2. Performance Comparison between the Optimal and Original Model

To ensure dynamic response capabilities, consideration should be given to the system's dynamic characteristic requirements by the requirements of the hydraulic servo motor control technique. The point (0.073, 46.81%, 21,234) in the Pareto front is selected as the optimal design, and its corresponding design variables are shown in Table 1. The LBPRM-EHSPCS test platform (see Figure 11) is built to evaluate the viability and efficacy of the suggested theory.

Table 1. Optimum decision variables and objective functions of the LBPRM-EHSPCS.

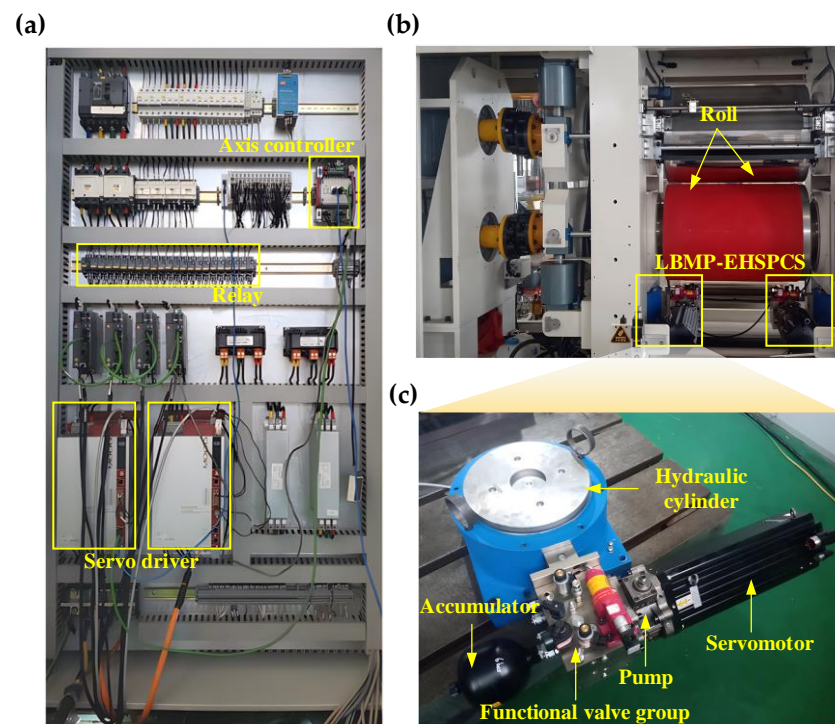| Objective Function			Design Variables		
$1/f$ (s)	$1-\eta$(%)	R_{hard} (¥)	T_e (N·m)	D_p (mL/r)	A_L (m^2)
0.73	46.81%	21,234	72	5.74	0.146

(a)

(b)

(c)

Figure 11. Experiment setup of the LBPRM-EHSPCS: (**a**) Electrical cabinet; (**b**) LBPRM; (**c**) LBPRM-EHSPCS.

The LBPRM is demonstrated in Figure 11b; the rolling mill pulls the battery pole piece into the rotating rollers by utilizing the friction between the rolls and the piece. To compress the pole piece to the required thickness, the EHSPCS modifies the distance between the two rollers. The parameters of the LBPRM are shown in Table 2. Especially, the EHSPCS is fixed on the lower roll on both ends of the LBPRM. The main components of the LBPRM-EHSPCS test platform are hardware and software. As shown in Figure 11c, the hardware consists of a hydraulic pump and an EPU (servo motor, fixed-displacement pump, accumulator, and functional valve group). A servo driver, relay, axis controller, and other components make up the program (Figure 11a).

Table 2. Parameters of the LBPRM.

Technical Parameter	Value
Pole piece	anode
Roll size	$\Phi\,125 \times 900$ mm
Rolling line speed (variable frequency speed regulation)	10–100 m/min
Maximum pressure of the master cylinder	470 t
The maximum pulling force of the bent cylinder	160 t
Roll gap adjustment range	0–2 mm
Roller gap adjustment accuracy (online)	0.001 mm
Pole piece width	300–800 mm
Pole piece thickness	0.1–0.25 mm
Radial runout of the roll loader	$< \pm 0.002$ mm

So long as the PMSM is operating, the driver can keep an eye on the motor's operational parameters, such as the torque and speed outputs, as well as the inputs of current and voltage. These parameters are fed back to the computer by the driver and the appropriate curves are generated. The valve block is equipped with pressure/flow sensors to measure the pressure and flow of the system. To gather the hydraulic cylinder's speed and force, the displacement/force sensors are integrated into the hydraulic cylinder. By returning these

numerical values to the computer through the controller, the sensor causes the program to create curves.

The external load force is fixed at 70 kN while the system is in its steady-state configuration. The efficiency characteristics of the key components and the system before and after optimization are obtained, which are shown in Figure 12. From Figure 12, the efficiency of the servomotor, fixed displacement pump, and hydraulic cylinder is increased by 2.2%, 4.6%, and 4.0%, respectively. The system efficiency is increased by as much as 7.2%, which may be attributed to the greater increase in the fixed displacement pump efficiency. Meanwhile, the improved efficiency of the LBPRM-EHSPCS will increase the lithium-ion battery manufacturing performance significantly. Additionally, the rising "S" slope trajectory signal is carried out to verify the dynamic response of the LBPRM-EHSPCS. Especially, the "S" slope trajectory displays displacements of 50 mm from 82.06 to 82.11 mm, and 100 mm from 82.06 to 82.16 mm. The corresponding displacement curves before and after optimization are achieved in Figure 13. From Figure 13a,b, the steady–state precision of the system is relatively inadequate. The displacement error reaches 0.008 and 0.016 mm, respectively, before optimization. Conversely, the steady-state accuracy is high with low overshoot (about 0.002 mm) after optimization. Thus, the lithium-ion battery manufacturing precision is enhanced. In all, the efficiency and dynamic characteristics of the LBPRM-EHSPCS are improved to a certain extent, which verifies the reliability of the proposed MOO for the LBPRM-EHSPCS. Furthermore, high-quality and good-efficiency new energy vehicle production is obtained.

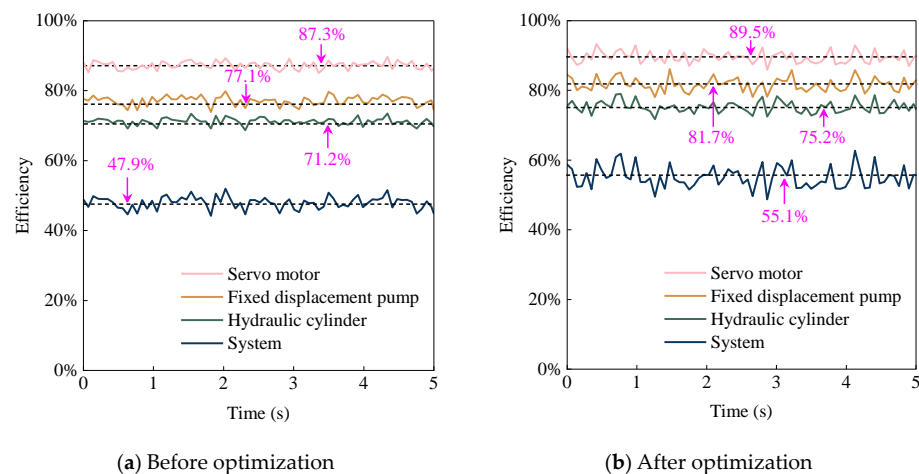(**a**) Before optimization   (**b**) After optimization

Figure 12. Efficiency characteristics comparison before and after optimization.
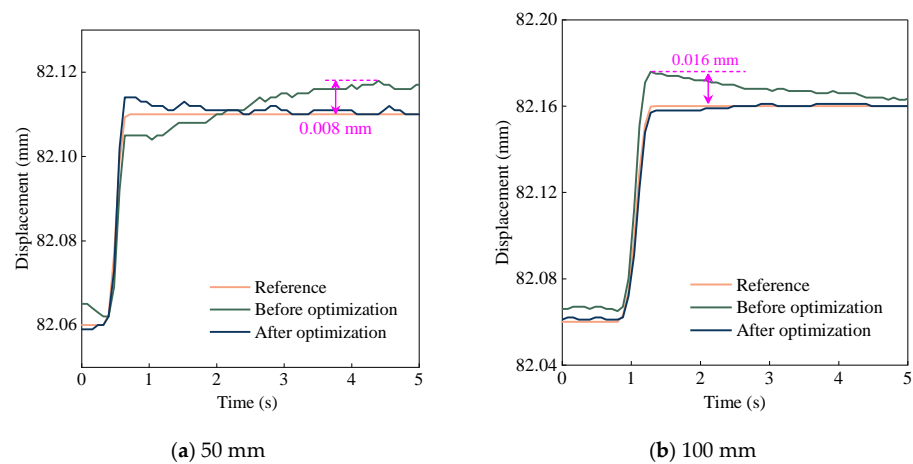

(**a**) 50 mm   (**b**) 100 mm

Figure 13. Dynamic characteristics comparison before and after optimization.

5. Conclusions

The valuable kinetic characteristics parameters of the LBPRM-EHSPCS are updated in the current work. Based on this, the Pareto front with the largest dynamic response, the least amount of power loss, and the lowest cost is achieved by the implementation of the NSGA-II algorithm. In conclusion, an analysis is conducted on the efficiency and dynamic properties of both the optimal and initial solution models.

According to the study, the servo motor torque, fix-displacement pump displacement, and hydraulic cylinder working area have the greatest influence on the dynamic, efficiency, and economic characteristics. These three dimensions are therefore regarded as the MOO problem's decision variables. Additionally, the kinetic characteristics of the original and the optimized model from the NSGA-II Pareto front are assessed. According to the findings, when compared to the baseline model, the optimal model greatly improves steady-state accuracy by increasing efficiency by 7.2%.

The MOO model of this study encourages researchers and engineers to quickly design and optimize the design parameter of the LBPRM-EHSPCS. Simultaneously, there are several limitations in this study: (1) although the NSGA-II algorithm reveals good performance in the optimization of the MOO problem, its optimized ability is worth further verification compared with more advanced algorithms and (2) the effect of the optimized structure on the lifespan and reliability of the LBPRM-EHSPCS also require to be investigated. These limitations will be addressed seriously in future studies.

Author Contributions: Formal analysis, Y.Z.; Funding acquisition, G.C.; Methodology, Y.Z. and G.Y.; Project administration, G.C. and W.J.; Resources, G.C. and G.Y.; Software, Y.Z. and B.L.; Supervision, G.C. and W.J.; Writing—original draft, Y.Z. and B.L.; Writing—review & editing, Y.Z. and J.L. All authors have read and agreed to the published version of the manuscript.

Data Availability Statement: Not applicable.

Conflicts of Interest: The authors declare no conflict of interest.

Abbreviations

EHSPCS	Electro-hydraulic servo pump control system
EHSV	Electro-hydraulic servo valve
EHSV-AGC	Electro-hydraulic servo valve automatic gauge control
Gen	Generation
HAGC	Hydraulic automatic gauge control
HV	Hypervolume
LBPRM	Lithium-ion battery pole rolling mill
MOO	Multi-objective optimization
NSGA-II	Non-dominated sorting genetic algorithm II

Nomenclature

B	Sinusoidal signal amplitude
f	Sinusoidal signal frequency (Hz)
x_L	Hydraulic cylinder displacement (m)
t	Hydraulic cylinder displacement time (s)
v_L	Hydraulic cylinder operating speed (m/s)
γ	Attenuated percentage of the sinusoidal signal amplitude
F_L	Hydraulic cylinder load force (N)
M	Load (kg)
a_L	Hydraulic cylinder operating acceleration (m/s^2)
P_L	Hydraulic cylinder required power (W)
Q_L	Hydraulic cylinder required flow rate (m^3/s)
A_L	Hydraulic cylinder working area (m^2)

Q	Fixed-displacement pump theoretical output flow (m^3/s)
D_p	Fixed-displacement pump displacement (mL/r)
w	Servo motor angular velocity (rad/s)
n	Servo motor speed (rpm)
α	Servo motor angular acceleration (rad/s^2)
T_e	Servo motor electromagnetic torque (N·m)
J_{mp}	Motor pump group rotor inertia (kg·m^2)
P	Servo motor required power (W)
T_L	Servo motor equivalent load torque (N·m)
P_{Fe}	Stator iron loss (W)
P_c	Eddy current loss (W)
P_h	Hysteresis loss (W)
P_e	Additional loss (W)
k_c	Eddy current loss coefficient
f_1	Alternating magnetic field frequency (Hz)
B_{m1}	Magnetic density (T)
k_h	Hysteresis loss coefficient
b_1	Steinmetz coefficient
k_e	Additional loss coefficient
P_{Cu}	Winding copper loss (W)
m	Motor phase
I	Motor phase current effective value (A)
R	Each phase resistance (W)
P_m	Mechanical power loss (W)
k_r	Rotor surface roughness
ρ	Gas density (kg/m^3)
C_m	Friction coefficient
r	Rotor radius (m)
l	Rotor axial length (m)
P_{loss}^{motor}	Servo motor total power loss (W)
Q_{L1}	Release between the plunger and the cylinder block (m^3/s)
d_p	Plunger diameter (m)
δ_p	Gap between the plunger and the inner wall of the cylinder bore (m)
Δp_1	Pressure drop of the piston pump (MPa)
μ	Oil dynamic viscosity (Pa·s)
L_p	Length of contact between the plunger and the cylinder bore (m)
ε	Eccentricity
Q_{L2}	Leakage between the slip shoe and the stator (m^3/s)
h	Thickness of the oil film between the stator and the shoe (m)
r_1	Inner radius of the shoe sealing belt (m)
r_2	Outer radius of the shoe sealing belt (m)
Q_{L3}	Leakage of the distribution shaft and rotor (m^3/s)
f_v	Leaking packet corners
r_v	Distribution shaft radius (m)
δ_v	Clearance between the plunger and the rotor (m)
L_v	Contact length (m)
P_{f1}	Plunger pair friction loses power (W)
F_{f1}	Plunger pair friction (N)
d_p	Plunger diameter (m)
δ_1	Clearance between the plunger and the cylinder block (m)
L_p	Plunger width (m)
P_{f2}	Distribution pair friction loses power (W)
T_{f2}	Distribution shaft torque (N·m)
w_2	Stator speed (rad/s)

P_{f3}	Distribution pair friction loses power (W)
T_{f3}	Distribution shaft torque (N·m)
w_3	Rotor speed (rad/s)
P_{loss}^{pump}	Fixed-displacement pump total power loss (W)
N	Number of plunger pump plungers
Q_{Lc}	Hydraulic cylinder leakage (m^3/s)
Δp_2	Pressure drop of the cylinder two cavity (MPa)
v_c	Piston rod speed (m/s)
F_{fc}	Friction force experienced by the piston (N)
d_c	Hydraulic cylinder piston diameter (m)
l_c	Length of internal wall gap between piston and cylinder (m)
h_c	Height of internal wall gap between piston and cylinder (m)
P_0	Input power of the servo motor shaft (W)
k_t	Torque constant (N·m)
η_v	Pump volumetric efficiency (%)
η_{mp}	Pump mechanical efficiency (%)
η_p	Pump total efficiency (%)
η_{hc}	Hydraulic cylinder efficiency (%)
η	System total efficiency (%)
η_m	Servo motor total efficiency (%)
R_{hard}	Hardware cost (¥)
R_{motor}	Servo motor cost (¥)
R_{pump}	Fixed-displacement pump cost (¥)
$R_{cylinder}$	Hydraulic cylinder cost (¥)
a_1, a_2, a_3	Curve-fitting parameter of the servo motor cost
b_1, b_2, b_3	Curve-fitting parameter of the fixed-displacement pump
c_1, c_2, c_3	Curve-fitting parameter of the hydraulic cylinder
P_t	Random population
M	Population size
d_i	Crowding distance of individuals
k	Objective function number
f_j^{i+1}	Objective function j of individuals i+1
f_j^{i-1}	Objective function j of individuals i-1
f_j^{max}	Maximum value of objective function j
f_j^{min}	Minimum value of objective function j
Q_t	Subsample population

References

1. Gholipour, M.R.; Saradarzadeh, M.; Farhangi, S. Wireless power transfer pulse charging of lithium-ion battery. *J. Energy Storage* **2023**, *72*, 108402. [CrossRef]
2. Miao, Y.; Liu, L.; Zhang, Y.; Tan, Q.; Li, J. An overview of global power lithium-ion batteries and associated critical metal recycling. *J. Hazard. Mater.* **2022**, *425*, 127900. [CrossRef]
3. Jie, G.; Liangheng, Z.; Yan, L.; Fan, S.; Bin, W.; Cunfu, H. Ultrasonic guided wave measurement and modeling analysis of the state of charge for lithium-ion battery. *J. Energy Storage* **2023**, *72*, 108384. [CrossRef]
4. Wang, C.; Yang, F.; Vo, N.T.M.; Nguyen, V.T.T. Enhancing Lithium-Ion Battery Manufacturing Efficiency: A Comparative Analysis Using DEA Malmquist and Epsilon-Based Measures. *Batteries* **2023**, *9*, 317. [CrossRef]
5. Bridge, G.; Faigen, E. Towards the lithium-ion battery production network: Thinking beyond mineral supply chains. *Energy Res. Soc. Sci.* **2022**, *89*, 102659. [CrossRef]
6. Li, C.; Zhang, H.; Ding, P.; Yang, S.; Bai, Y. Deep feature extraction in lifetime prognostics of lithium-ion batteries: Advances, challenges and perspectives. *Renew. Sustain. Energy Rev.* **2023**, *184*, 113576. [CrossRef]
7. Xu, J.; Xie, S.; Lin, Z.; Qiu, X.; Wu, K.; Zheng, H. Studies of interfacial reaction characteristics for high power lithium-ion battery. *Electrochim. Acta* **2022**, *435*, 141305. [CrossRef]
8. Wu, M.; Qin, L.; Wu, G. State of charge estimation of Power lithium-ion battery based on an Affine Iterative Adaptive Extended Kalman Filter. *J. Energy Storage* **2022**, *51*, 104472. [CrossRef]

9. Gottschalk, L.; Strzelczyk, N.; Adam, A.; Kwade, A. Influence of different anode active materials and blends on the performance and fast-charging capability of lithium-ion battery cells. *J. Energy Storage* **2023**, *68*, 107706. [CrossRef]

10. Pistorio, F.; Clerici, D.; Mocera, F.; Somà, A. Review on the numerical modeling of fracture in active materials for lithium ion batteries. *J. Power Sources* **2023**, *566*, 232875. [CrossRef]

11. Lundkvist, A.; Larsson, P.-L.; Olsson, E. A discrete element analysis of the mechanical behaviour of a lithium-ion battery electrode active layer. *Powder Technol.* **2023**, *425*, 118574. [CrossRef]

12. Qi, L.; Wang, Y.; Kong, L.; Yi, M.; Song, J.; Hao, D.; Zhou, X.; Zhang, Z.; Yan, J. Manufacturing processes and recycling technology of automotive lithium-ion battery: A review. *J. Energy Storage* **2023**, *67*, 107533. [CrossRef]

13. Li, L.; Gu, Z.; Xu, W.; Tan, Y.; Fan, X.; Tan, D. Mixing mass transfer mechanism and dynamic control of gas-liquid-solid multiphase flow based on VOF-DEM coupling. *Energy* **2023**, *272*, 127015. [CrossRef]

14. Cao, M.; Wang, L.; Zhang, Q.; Zhang, H.; Zhong, S.; Chen, J. Boosting the comprehensive behaviors of $LiNi_{0.5}Co_{0.2}Mn_{0.3}O_2$ lithium-ion batteries via CNTs/Super-P composite conductive agent. *Mater. Today Commun.* **2023**, *36*, 106677. [CrossRef]

15. He, X.; Fang, S.; Li, Z.; Wu, Z.; Liu, Y.; Liu, Y.; Gao, M.; Du, W.; Yang, Y. Constructing a conductive and buffer network on microscale silicon-based anodes for high-performance lithium-ion batteries. *J. Alloys Compd.* **2023**, *949*, 169846. [CrossRef]

16. Li, L.; Xu, W.; Tan, Y.; Yang, Y.; Yang, J.; Tan, D. Fluid-induced vibration evolution mechanism of multiphase free sink vortex and the multi-source vibration sensing method. *Mech. Syst. Signal Process.* **2023**, *189*, 110058. [CrossRef]

17. Zhu, Y.; Tang, S.; Wang, C.; Jiang, W.; Zhao, J.; Li, G. Absolute Stability Condition Derivation for Position Closed-Loop System in Hydraulic Automatic Gauge Control. *Processes* **2019**, *7*, 766. [CrossRef]

18. Dong, M.; Liu, C.; Li, G. Robust Fault Diagnosis Based on Nonlinear Model of Hydraulic Gauge Control System on Rolling Mill. *IEEE Trans. Control Syst. Technol.* **2010**, *18*, 510–515. [CrossRef]

19. Prinz, K.; Steinboeck, A.; Kugi, A. Optimization-based feedforward control of the strip thickness profile in hot strip rolling. *J. Process Control* **2018**, *64*, 100–111. [CrossRef]

20. Wang, Y.; Wang, M.; Fu, J.; Fu, Y. Adaptive Control of an Aerospace Electrohydrostatic Actuator with a Constant-Torque Variable-Displacement Pump. *J. Aerosp. Eng.* **2022**, *35*, 04022028. [CrossRef]

21. Kumar, M. A survey on electro hydrostatic actuator: Architecture and way ahead. *Mater. Today Proc.* **2021**, *45*, 6057–6063. [CrossRef]

22. Fu, Y.; Han, X.; Sepehri, N.; Zhou, G.; Fu, J.; Yu, L.; Yang, R. Design and performance analysis of position-based impedance control for an electrohydrostatic actuation system. *Chin. J. Aeronaut.* **2018**, *31*, 584–596. [CrossRef]

23. Yin, X.; Zhang, W.; Jiang, Z.; Pan, L. Adaptive robust integral sliding mode pitch angle control of an electro-hydraulic servo pitch system for wind turbine. *Mech. Syst. Signal Process.* **2019**, *133*, 105704. [CrossRef]

24. Do, T.C.; Dang, T.D.; Dinh, T.Q.; Ahn, K.K. Developments in energy regeneration technologies for hydraulic excavators: A review. *Renew. Sustain. Energy Rev.* **2021**, *145*, 111076. [CrossRef]

25. Guo, Q.; Chen, Z.; Shi, Y.; Li, X.; Yan, Y.; Guo, F.; Li, S. Synchronous control for multiple electrohydraulic actuators with feedback linearization. *Mech. Syst. Signal Process.* **2022**, *178*, 109280. [CrossRef]

26. Jiao, Z.; Wang, Z.; Liu, X.; Wang, H.; Qi, P.; Qiao, W. Multi-parameter load sensing pump model simulation and flow rate characteristics research. *Chin. J. Aeronaut.* **2022**, *35*, 296–308. [CrossRef]

27. Wang, F.; Chen, G.; Liu, H.; Yan, G.; Zhang, T.; Liu, K.; Liu, Y.; Ai, C. Research on Position Control of an Electro–Hydraulic Servo Closed Pump Control System. *Processes* **2022**, *10*, 1674. [CrossRef]

28. Yao, J.; Wang, P.; Dong, Z.; Jiang, D.; Sha, T. A novel architecture of electro-hydrostatic actuator with digital distribution. *Chin. J. Aeronaut.* **2021**, *34*, 224–238. [CrossRef]

29. Mesalhy, O.; Elsayed, M.L.; Corona, J.J., Jr.; Kwarteng, A.A.; Kizito, J.P.; Leland, Q.H.; Chow, L.C. Study of a high-reliability dual-fan system for cooling aerospace electromechanical actuators. *Therm. Sci. Eng. Prog.* **2020**, *18*, 100540. [CrossRef]

30. Yang, M.; Chen, G.; Lu, J.; Yu, C.; Yan, G.; Ai, C.; Li, Y. Research on Energy Transmission Mechanism of the Electro-Hydraulic Servo Pump Control System. *Energies* **2021**, *14*, 4869. [CrossRef]

31. Yan, G.; Jin, Z.; Zhang, T.; Zhang, C.; Ai, C.; Chen, G. Exploring the Essence of Servo Pump Control. *Processes* **2022**, *10*, 786. [CrossRef]

32. Fan, Y.; Lyu, P.; Zhan, D.; Ouyang, K.; Tan, X.; Li, J. Surrogate model-based multiobjective design optimization for air-cooled battery thermal management systems. *Eng. Appl. Comput. Fluid Mech.* **2022**, *16*, 1031–1047. [CrossRef]

33. Jiang, J.; Cai, H.; Ma, C.; Qian, Z.; Chen, K.; Wu, P. A ship propeller design methodology of multi-objective optimization considering fluid–structure interaction. *Eng. Appl. Comput. Fluid Mech.* **2018**, *12*, 28–40. [CrossRef]

34. Zhang, J.; Shen, Y.; Gan, M.; Su, Q.; Lyu, F.; Xu, B.; Chen, Y. Multi-objective optimization of surface texture for the slipper/swash plate interface in EHA pumps. *Front. Mech. Eng.* **2022**, *17*, 48. [CrossRef]

35. Zong, C.; Li, Q.; Li, K.; Song, X.; Chen, D.; Li, X.; Wang, X. Computational fluid dynamics analysis and extended adaptive hybrid functions model-based design optimization of an explosion-proof safety valve. *Eng. Appl. Comput. Fluid Mech.* **2022**, *16*, 296–315. [CrossRef]

36. Wang, C.-N.; Yang, F.-C.; Nguyen, V.T.T.; Vo, N.T.M. CFD Analysis and Optimum Design for a Centrifugal Pump Using an Effectively Artificial Intelligent Algorithm. *Micromachines* **2022**, *13*, 1208. [CrossRef]

37. Yang, M.; Zhang, Y.; Ai, C.; Yan, G.; Jiang, W. Multi-objective optimisation of K-shape notch multi-way spool valve using CFD analysis, discharge area parameter model, and NSGA-II algorithm. *Eng. Appl. Comput. Fluid Mech.* **2023**, *17*, 2242721. [CrossRef]

38. Yang, M.; Yan, G.; Zhang, Y.; Zhang, T.; Ai, C. Research on high efficiency and high dynamic optimal matching of the electro-hydraulic servo pump control system based on NSGA-II. *Heliyon* **2023**, *9*, e13805. [CrossRef]

39. Tian, Y.; Zhu, W.; Zhang, X.; Jin, Y. A practical tutorial on solving optimization problems via PlatEMO. *Neurocomputing* **2023**, *518*, 190–205. [CrossRef]